Superior Performance of V_2O_5 as Hole Selective Contact over other Transition Metal Oxides in Silicon Heterojunction Solar Cells

Osbel Almora[1], Luis G. Gerling[2,3], Cristóbal Voz[2], Ramón Alcubilla[2,3], Joaquim Puigdollers[2,3,*], and Germà Garcia-Belmonte[1,*]

[1] *Institute of Advanced Materials (INAM), Universitat Jaume I, 12006 Castelló, Spain*

[2] *Electronic Engineering Department, Universitat Politècnica de Catalunya, Jordi Girona 1–3, Barcelona 08034, Spain*

[3] *Centre de Recerca en Nanoenginyeria (CrNE), Pascual Vila 15, Barcelona 08028, Spain*

Abstract

Transition metal oxides (TMOs) have recently been proved to efficiently serve as hole-selective contacts in crystalline silicon (c-Si) heterojunction solar cells. In the present work, two TMO/c-Si heterojunctions are explored using MoO_3 (reference) and V_2O_5 as an alternative candidate. It has been found that V_2O_5 devices present larger (16% improvement) power conversion efficiency mainly due to their higher open-circuit voltage. While V_2O_5/c-Si devices with textured front surfaces exhibit larger short-circuit currents, it is also observed that flat solar cell architectures allow for passivation of the V_2O_5/n-Si interface, giving significant carrier lifetimes of 200 μs (equivalent to a surface recombination velocity of S_{eff} ~140 cm s^{-1}) as derived from impedance analysis. As a consequence, a significant open-circuit voltage of 662 mV is achieved. It is found that, at the TMO/c-Si contact, a TMO work function enhancement $\Delta\Phi_{TMO}$ occurs during the heterojunction formation with its consequent dipole layer enlargement $\Delta'=\Delta+\Delta\Phi_{TMO}$. Our results provide new insights into the TMO/c-Si contact energetics, carrier transport across the interface and surface recombination allowing for further understanding of the nature of TMO/c-Si heterojunctions.

Keywords: Transition metal oxides, silicon solar cells, impedance spectroscopy, passivation, minority carrier lifetime.

*Corresponding authors:

J. Puigdollers, (joaquim.puigdollers@upc.edu) tel.:+34 93 4011002

G. Garcia-Belmonte, (garciag@uji.es) tel.: +34 964 387538

30 November 2017

1. Introduction

During the last decade, crystalline silicon (c-Si) heterojunction solar cells incorporating thin films of hydrogenated amorphous silicon (a-Si:H) have become the state-of-the-art photovoltaic technology, achieving record efficiencies above 26% [1]. The key for the success of this technology lies on the superior surface passivation provided by very thin layers (<5 nm) of intrinsic a-Si:H, also allowing for carrier conduction with minimal resistive losses. However, performance limitations caused by the relatively high optical absorption of a-Si:H [2] and the highly recombining *n/p* doped layers [3] (which act as electron/hole selective contacts) have led to investigate novel heterojunction concepts between c-Si and dopant-free highly-transparent transition metal oxides (TMOs) [4, 5].

Originally introduced in organic electronics as electron and hole transport layers, TMOs are large band gap (E_g >3 eV) semiconductors with a wide variety of work functions (Φ_{TMO}~3–7 eV) and conductivities (from insulating to metallic-like), providing great flexibility when used as electron- or hole-selective contact materials [6]. Additionally, they can be deposited at low temperature (T <200ºC) or by solution-processing methods [7], increasing the potential for process simplification and cost reduction. Until now, hole-selective MoO_3 has been the study-case TMO material alongside n-type crystalline silicon (n-Si), reaching a power conversion efficiency (*PCE*) of 22.5% in a MoO_3/(i)a-Si:H/n-Si configuration [8], where the intrinsic (i)a-Si:H chemically passivates the silicon surface while MoO_3 provides the hole-selectivity. Also rear MoO_x contacts with partial contact areas have been reported with an efficiency of 20.4% [9]. As an alternative, simpler structures comprising TMOs in direct contact with n-Si have also been proposed, achieving efficiencies between 12.5 and 18.4% [10-12].

The unique behavior of MoO_3 and other similar TMOs (V_2O_5, WO_3) is explained by their electronic configuration and large work function values (Φ_{TMO}>5.0 eV), which upon Fermi level (E_F) alignment with n-Si ($\Phi_{n\text{-}Si}$~4.2 eV) induces a potential barrier (band bending) [10, 13]. This is believed to result in the formation of an inversion (p^+) layer upon n-Si where photogenerated holes are collected and then extracted across the TMO/n-Si interface. Recent reports have also proposed V_2O_5 as an interesting alternative to MoO_3, indicating that larger open-circuit voltage values (higher hole-selectivity) can be achieved for V_2O_5–based devices with and without the inclusion of passivating (i)a-Si:H interlayers [10-12].

In the present paper, Impedance Spectroscopy (*IS*) measurements were used to compare the performance of MoO_3 and V_2O_5 as hole-selective contacts in n-Si solar cells, showing that V_2O_5–based solar cells perform better due to the presence of higher built-in voltages. Additionally, temperature-dependent measurements were used to calculate barrier heights across the interface, giving further details about the energetics of TMO/n-Si heterojunctions.

2. Experimental

Devices Fabrication: Solar cells were fabricated from n-type 2 Ω·cm resistivity wafers (~2.3×10^{15} cm^{-3} dopant concentration) made from float zone monocrystalline (100 orientation) material. The use of such high quality silicon allows for a very high bulk lifetime (τ_{bulk} ~3 ms under high injection conditions), ensuring almost all recombination effects are confined to the surfaces. Solar cells labeled t-MoO_3 and t-V_2O_5 were subjected to random texturization of the front surface by alkaline etching (~265 μm final wafer thickness), while cells named f-V_2O_5 were processed as purchased (flat polished finish, ~280 μm wafer thickness). After a standard RCA cleaning 1% HF dip, all substrates were then loaded into a plasma-enhanced chemical vapor deposition (PECVD) system to deposit on the rear side an electron-selective contact consisting of an intrinsic/n-type a-SiC_x:H stack (5 nm/15 nm, x~0.2). Subsequently, two rear contact strategies were used: *1)* t-MoO_3 and t-V_2O_5 cells had an a-SiC_x:H back-reflector (80 nm, x~1) deposited by PECVD which was then laser-fired to obtain an array of locally-diffused point contacts (0.5% contacted area) [14]; *2)* f-V_2O_5 cells had an indium-tin-oxide (ITO) back-reflector/electrode deposited by RF magnetron sputtering (80 nm, 1.3×10^{-3} mbar Ar pressure). As for the front hole-selective contacts, 20 nm thick TMO films were thermally evaporated from powdered V_2O_5/MoO_3 sources (>99.99% purity, Sigma Aldrich) at ~8×10^{-6} mbar. For the front textured sample, the deposition time was ~1.7 times longer than the polished ones, in order to compensate for the increase in surface area. The deposition rate was ~0.2 Å/s, as controlled by quartz micro-balance, while the substrate remained at room temperature during the process. After a brief air exposure, an ITO front electrode/antireflective layer (80 nm) was also deposited. At this point in the process, QSSPC measurements were performed in order to determine the carrier lifetime of the solar cell precursor (figure S5). After lithographic patterning of 1 cm^2 active cell areas, a front-contact Ag grid (4.3% shadow losses) was thermally evaporated by use of a shadow mask, while the back-contact metallization was done by e-beam evaporation of Ti/Al (t-MoO_3 and t-V_2O_5) or Ag evaporation (f-V_2O_5).

Characterizations: The *IS* measurements at V_{oc} (Figures S7-S9) were carried out using an Autolab PGSTAT-30 potentiostat in the frequency range between 100 mHz and 1 MHz, being the AC perturbation of 10 mV. The spectra were recorded in open-circuit conditions under varying illumination up to 150 mW cm^{-2} (XE 300W Newport 6258). For achieving this, a bias voltage which corresponds to V_{oc} was applied, hence ensuring a more homogeneous distribution of excess carriers by suppressing DC current. For practical reasons, an extra loop element was included in series connection with the circuit (Figure 5a), and at some spectra a constant phase element was considered instead of a second capacitor. For the *IS* measurements at short-circuit in the dark and at different temperatures (Figure S3), a Gamry Reference 3000 potentiostat/galvanostat/ZRA (same AC perturbation and frequency range as above) was employed joining the Novocontrol Quatro Cryosystem.

3. Results and discussion

3.1 Device structures and performance

The structure of the three representative devices studied here is presented in the sketches of Figure 1, including the specifications about composition and thickness of each layer. This set of configurations will allow us to properly compare performances among V_2O_5– and MoO_3–based Si heterojunction solar cells. The first structure, labeled t-MoO_3, uses a 20 nm-thick layer of MoO_3 as front hole-selective contact deposited on a textured surface, while the rear electron-selective contact is formed by a (i/n^+)a-$SiC_{x\sim0.2}$:H stack that was locally-diffused by laser firing (Figure 1a). On the other hand, there are two structures with V_2O_5 as hole selective contact called t-V_2O_5 and f-V_2O_5 (see Figures 1b and 1c, respectively). While t-V_2O_5 presents the same structure as t-MoO_3, f-V_2O_5 exhibits a flat superposition of layers, increasing the passivation quality provided by V_2O_5. Moreover, f-V_2O_5 uses indium tin oxide (ITO) as a rear electrode, given that laser firing provides a good ohmic contact at the expense of reduced passivation quality. More details about the devices fabrication and morphological features can be found in previous works [10, 15], the experimental section and the Supplementary Information (SI).

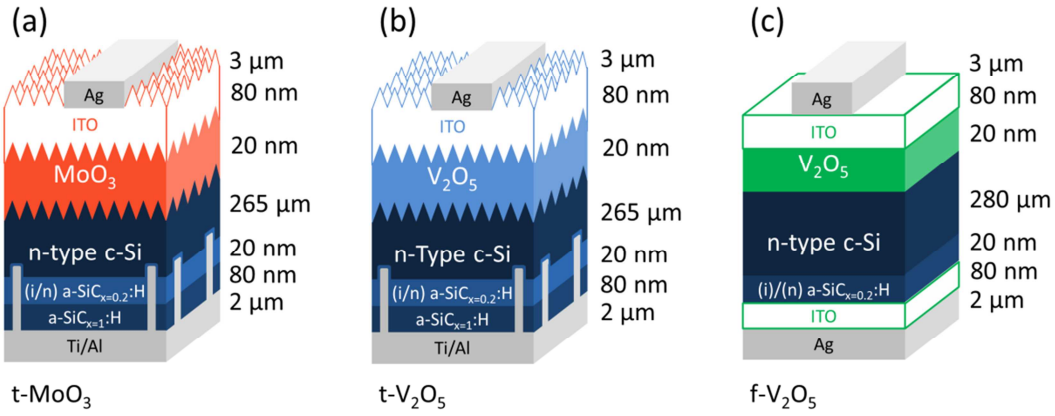

Figure 1: Sketches of the structures for the three devices which were studied in this work, as indicated.

Examples of current density-voltage (*J-V*) curves resulting from representative devices measured under illumination are shown in Figure 2. The corresponding performance parameters such as open-circuit voltage (V_{oc}), short-circuit current (J_{sc}), fill factor (*FF*) and *PCE* are summarized in Table 1. Also histograms in Figure S1 present the parameter distribution for the complete set of studied samples. In this respect, devices with V_2O_5 show significantly higher *PCE* than those comprising MoO_3 layers. Given that only minor improvements in the photocurrent generation and no clear trend in the *FF* are observed, the superiority of V_2O_5–based solar cells is directly connected to the enhancement in the output V_{oc} in comparison with MoO_3. Illustratively, among the samples with surface texturing (t-V_2O_5 and t-MoO_3), t-V_2O_5 has a larger J_{sc} while the flat sample (f-V_2O_5) has practically the same J_{sc} as t-MoO_3. Additionally, the

V_{oc} differences are apparent with significantly larger values achieved by the V_2O_5 devices. Our findings then indicate that the V_2O_5/n-Si heterojunction makes up a superior contact compared to MoO_3/n-Si.

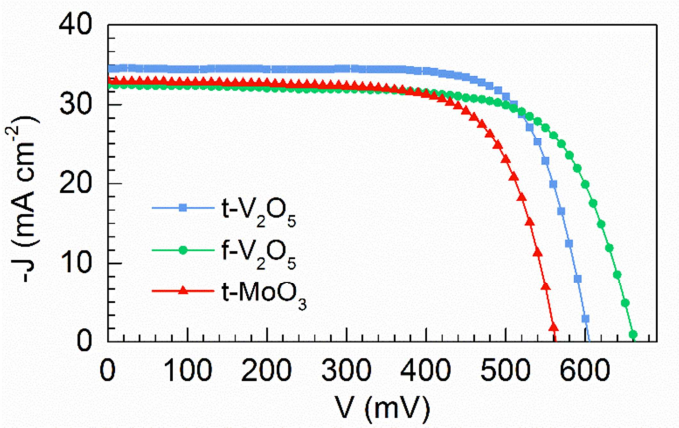

Figure 2: Experimental current density-voltage curves measured under 100 mW·cm^{-2} of AM1.5G light spectrum for different samples as indicated.

Table 1: Photovoltaic parameters corresponding to the *J-V* curves in Figure 2 and calculated parameters from the analysis of the *MS* plots in Figure 3. The depletion layer width w_0 is presented at zero bias and, in parenthesis, the value calculated for the real semiconductor doping (2.3×10^{15} cm^{-3}). This allows comparing deviations caused by geometric effects on the capacitance area normalization.

Devices	V_{oc} (mV)	J_{sc} (mA cm^{-2})	*FF* (%)	*PCE* (%)	V_{bi} (mV)	N_D ($\times10^{15}$ cm^{-3})	w_0 (nm)
t-MoO_3	563	33.0	72.1	13.4	599	4.37	406 (560)
t-V_2O_5	605	34.5	74.7	15.6	617	6.86	330 (569)
f-V_2O_5	662	32.5	70.6	15.2	712	2.10	644 (614)

3.2 TMO/n-Si heterojunction analysis.

The formation of the heterojunction in the TMO/n-Si devices occurs by band bending of the n-Si energy levels producing a built-in potential V_{bi}. However, before entering into a discussion of the energy band diagram, it is required to explore the depletion region features in order to estimate V_{bi} values exhibited by the devices. Therefore, capacitance measurements as a function of DC applied voltage in the dark were done. Figure 3 exhibits such results in the typical Mott-Schottky (MS) plot representation, i.e. $C^{-2}(V)$. The linear decrease of MS plots, as the applied voltage is swept from reverse bias to near flat band condition, evidences a constant charge density profile. Subsequently, the neutrality of charge between the negative ionized defects, presumably

at the thin TMO side, and the positive Si ionized impurities, allow us to assume the one side abrupt junction approximation [16]. Thus the depletion layer width *w* at the n-type silicon bulk can be calculated as a function of the applied DC bias *V* as

$$w = \sqrt{\frac{2\varepsilon_0\varepsilon}{qN_D}\left(V_{bi} - V - \frac{2k_BT}{q}\right)} \quad (1)$$

where q is the elementary charge, k_B is the Boltzmann constant, T is the absolute temperature, ε_0 is the vacuum permittivity, ε is the relative dielectric constant (11.9 for Si) [16, 17], and N_D is the donor density (doping concentration with negligible intrinsic defects). The $2k_BT/q$ term corresponds to the majority-carrier contribution in addition to the impurity concentration [16]. With this in mind, a parallel-plate capacitor model can be considered for the determination of the depletion layer capacitance per unit area as $C_{dl} = \varepsilon_0\varepsilon / w$. Subsequently, by substituting equation 1 and after a few operations, the simplest expression for MS analysis is obtained as

$$C_{dl}^{-2} = \frac{2}{q\varepsilon_0\varepsilon N_D}\left(V_{bi} - V - \frac{2k_BT}{q}\right). \quad (2)$$

The V_{bi} can be obtained from the voltage intercept while N_D results from the slope of the linear portion in $C^{-2}(V)$. By substituting these results in equation (1), *w* at a given applied bias can be obtained. Resulting values for V_{bi}, N_D and w_0 (at V=0) are reported here for the first time for TMO/c-Si solar cells, showing the expected behavior characteristic of p-n junctions (see Table 1). Regarding the band bending, it accords well with previous experimental reports via Surface Photovoltage (SPV) and theoretical simulations for the $\Phi_{n\text{-}Si}$ range [11, 18]. N_D and w_0 values in Table 1 are also in good agreement with typical orders of magnitude observed in similar structures, although they do not consider effective area rectifications and/or contributions from gap trapping states. In fact, unlike the textured samples, the presence of gap defect levels is evidenced in the f-V_2O_5 device from its frequency dependent capacitance response [19, 20] shown in Figure S2, where the slope of the MS plot varies with the AC perturbation frequencies, even though they converge to the same V_{bi} value.

MS analysis straightforwardly gives V_{bi} as the intercept of the linear plots with the voltages axis, irrespective of area normalization or frequency dependent capacitances [16]. Similarly to the above mentioned V_{oc} behavior, devices with V_2O_5 present higher V_{bi} than those incorporating MoO_3, being f-V_2O_5 the structure with the larger value. Interestingly, the obtained V_{bi} values are similar to those of standard c-Si solar cells in which 600–750 mV are distributed between the two sides of the homojunction, suggesting that TMO/n-Si heterojunction behave similarly [21, 22]. The difference here is that $V_{bi} \sim$ 0.6–0.7 V is restricted to the Si side, indicating that the junction achieves weak inversion at zero bias. In addition, an almost ideal linear MS plot (Figures 3 and S2) is very much less frequent in heterojunction devices like CdTe [23, 24], CIGS [25, 26], organic [27] and hybrid [28] solar cells, where the constant doping profile (regular slope) is rarely reported. Since a constant charge density profile translates into a

quadratic behavior of the potential within *w*, a quadratic bending of the energy bands can also be expected. These two elements (large V_{bi} and constant doping) could support previous assumptions on the occurrence of a p-type inversion layer upon n-Si in the vicinity of the TMO interface (see energy-scaled band diagram of Figure 4a).

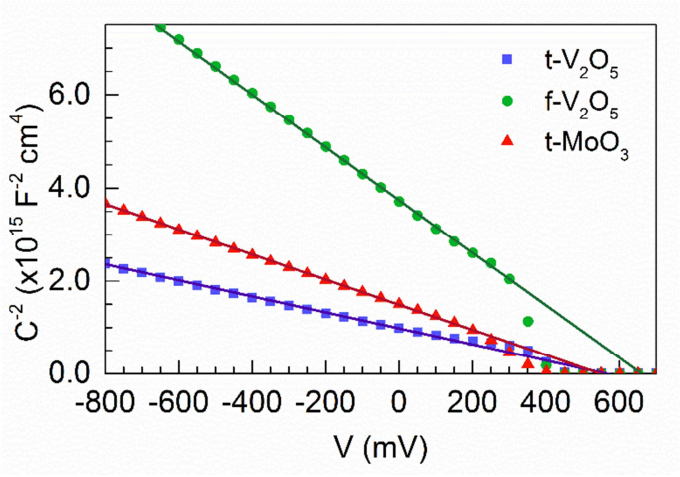

Figure 3: Experimental (dots) Mott-Schottky plots and respective linear fittings (lines) under dark and room temperature conditions for the different samples, as indicated. The AC perturbation was 10 mV at 1.0 kHz.

As summarized in Table ST1, the studied TMOs possess large energy bandgaps and work functions compared to silicon, and generally exhibit prominent n-type conductivity due to defect states generated from oxygen vacancies [6]. This is the reason why it has been proposed [10, 15] that a dipole layer Δ is present at the TMO/n-Si interface, in order to equilibrate the Fermi levels in the energy band diagram once the heterojunction is formed. Considering absolute values and assuming no significant changes in the TMO electron affinity after the contact is made, this can be written as

$$\Phi_{TMO} - \Phi_{n\text{-}Si} = qV_{bi} + \Delta . \qquad (3)$$

The spatial distribution of the work function offset is illustrated in Figure 4a-c in an illustrative typical case assuming Φ_{TMO} ~6.7 eV, where the interfacial dipole is possibly originated by shallow O vacancies in the TMO bulk [6, 10, 29]. Here, usually reported bandgaps (Table ST1) and our calculated V_{bi} values (Table T1) were used to sketch energy levels before and after the formation of the heterojunction, reveling two possible scenarios. In the first case, the conduction band (E_C) bends up forming a barrier of height ΔE_C of approximately $\sim 25 k_B T$ for electrons (Figure 4b), while in the second case no barrier is formed (Figure 4c). When such relative high barriers ($\Delta E_C > 10 k_B T$) are present, typically thermionic emission and/or tunneling are expected to occur [16]. Therefore, as it is known, the current density J_{TE} follows the expression

$$J_{TE} = \frac{A\,T^2}{\alpha}\exp[-\frac{q\varphi}{k_B T}]\left\{\exp[\frac{qV}{k_B T}]-1\right\} \quad (4)$$

where $k_B T$ is the thermal energy, A is the Richardson constant, $q\varphi$ the distance between E_F and the top of the barrier ($q\varphi > \Delta E_C$ in Figure 4b), and α is the relation between the rest mass and the effective mass (m_0 / m^*) when thermionic emission over the barrier is the dominating mechanism. Thus, it can be proved [30] that the resistance unit surface $R_0 = (dJ_{TE}/dV)^{-1}$ at zero applied bias follows the relation

$$R_0 = \alpha\frac{k_B}{qAT}\exp[\frac{q\varphi}{k_B T}]. \quad (5)$$

At this point it is useful to mention that when tunneling has a significant contributing role an extra term must be added to equation (4) and α can be written as a more complex expression. Furthermore, if tunneling is the dominating mechanism, R_0 cannot be easily reduced to equation (5) and the temperature should not exponentially affect R_0. However, that situation is only expected for high doping levels above $10^{19}\ cm^{-3}$ [30]. Conveniently, from equation (5) it is apparent that the linear fit of $Ln[qTR_0A/k_B]$ versus $q/k_B T$ yields an slope equaling φ and an intercept approaching $Ln[\alpha]$, allowing for testing underlying mechanisms as thermionic emission and/or tunneling across the barrier.

For this purpose, *J-V* curves and impedance spectroscopy (*IS*) analyses were carried out for the textured samples (t-V_2O_5 and t-MoO_3) in the dark and within the temperature range between 210 K and 295 K. The noisy response from f-V_2O_5 due to its large R_0 values prevented a reliable data processing. From the studied *J-V* curves (Figures S3a,b) the slope of the linear fittings around *V*=0 was calculated and subsequently $R_0 = (dJ/dV)^{-1}$ obtained. As for the impedance, a Nyquist plot (negative imaginary part of impedance $-Z''$ versus the real component Z') [31] was obtained from the *IS* measurements (Figures S3c,d), and fitted to the series connection of a resistance R_s and a simple *RC* equivalent circuit (inset Figure S3c), being R_0 the resistance of the arc.

The R_0 values obtained from *J-V* and *IS* measurements can be observed in Figure S3e. With these values, Figure 4d was elaborated and the barriers estimated at $q\varphi \approx 16$ meV for t-V_2O_5 and $q\varphi \approx 50$ meV for t-MoO_3. Consequently, since such barriers are in the order of $k_B T$ and $\alpha \approx 10^{10}$, thermionic emission is discarded as the main transport mechanism over the barrier. This could be interpreted implying that the energy band diagram sketched in Figure 4b with ΔE_C may occur only if tunneling is the dominating mechanism. Alternatively, it is also possible that no barrier occurs at all, as presented in the third sketch of Figure 4c. In this case, during the heterojunction formation, and due to inner bandgap defect levels, the TMO work function is augmented $\Delta\Phi_{TMO}$ as well as the dipole layer $\Delta' = \Delta + \Delta\Phi_{TMO}$ (assuming no electron affinity change), in such a way that no interfacial barrier occurs.

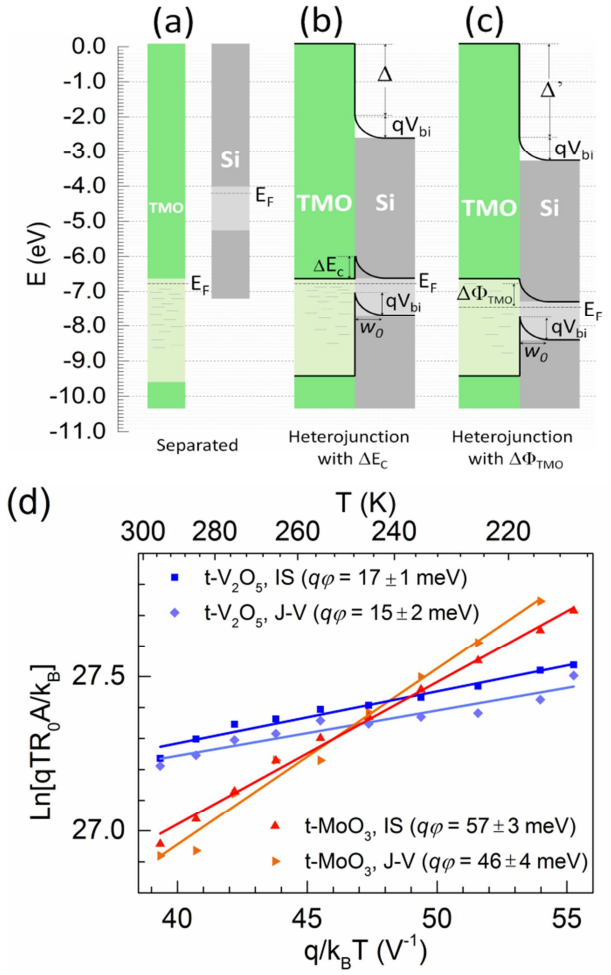

Figure 4: Energy band diagram for TMO and n-Si before contacting (a) and after the heterojunction formation with (b) and without (c) barrier formation ΔE_C. (d) Arrhenius plot with results for possible barriers φ for electrons. In (a) the zero signals the vacuum level and absolute values from tables T1 and ST1 were used. In (d) the data results from Figure S3 are considered. Here we propose a TMO work function enhancement $\Delta\Phi_{TMO}$ that also increases the dipole layer Δ and eliminates the barrier (c), provided that no electron affinity change occurs. This is possibly due to the absence of a barrier evidenced by the $q\varphi \approx k_B T$ values in (d).

Furthermore, there is also a work function scattering in Table ST1 that suggests a possible tunable conductivity in TMOs, which for V_2O_5 can reach almost the intrinsic state. The enhancement of the energetic offset between the E_F and the TMO conduction band minimum most probably depends on the n-Si surface defects and their passivation mechanisms, which is affected by fabrication conditions and reactivity, changing the TMO work function. In addition, another recent work [15] has pointed to the formation of a $SiO_{x\sim1.5}$ ultra-thin interlayer by chemical reaction between the TMO and the n-Si, as can be observed in Figure S4. This interlayer (not included in Figure 4b,c) can be directly holding the dipole or mediating the passivation. Nevertheless, work function tuning seems to be a more likely mechanism over barrier formation, at least for V_2O_5–

based devices. This is understood given V_2O_5's major Φ scattering (table ST1), their significantly higher V_{bi} and w_0 values (table T1) and the absence of a noteworthy barrier (Figure 4d). Such features may have a direct impact in the recombination mechanisms as studied in the following section.

3.3 Carrier lifetime by impedance analysis

The differences between V_2O_5– and MoO_3–based cells are also directly reflected in the contactless photo-conductance measurements in the quasi-steady state regime (QSSPC) [32], through which minority carrier lifetime results (Figure S5). Similarly to V_{oc} and V_{bi}, V_2O_5 samples show longer carrier lifetime values. However, the QSSPC technique does not account for contact effects since it is performed before the Ag grid deposition. Accordingly, a more suitable and general protocol is presented here for studying minority carrier lifetimes in TMO/n-Si solar cells, bearing in mind that differences with respect to the QSSPC technique may respond to the TMO role in the heterojunction formation and the top electrode.

In order to explore the dominating loss mechanism in these heterojunction–based devices, i.e. the so-called Shockley-Read-Hall (SRH) recombination through interface-located band gap states [33], *IS* analysis was used. Surface recombination proceeds by electron and hole capture by surface states with subsequent annihilation. The measurements were performed under illumination at open-circuit conditions. The equivalent circuit is presented in the inset of Figure 5a, where the experimental data of f-V_2O_5 at $V_{oc} = 633$ mV is also shown with its respective fitting. The circuit is basically composed by the series connection of a resistance R_s and two Voigt elements (parallel *RC* subcircuit, see Figure S6) [31]. In this sense, the SRH carrier lifetime results by summing terms related to the capture rate of electrons and holes in the surface recombination center [33]. Occupancy changes of conduction band electrons and valence band holes can be accessed by exploring capacitive effect of respective excess carriers. The usually-known diffusion capacitance [16] or chemical capacitance [34] C_n informs on the occupancy of conduction band bulk electrons [35]:

$$C_n = q^2 \frac{dn}{dE_{F_n}} \tag{6}$$

where the capacitance is given per unit volume, n corresponds to the free electron concentration and E_{F_n} accounts for the electron quasi-Fermi level. Since at forward bias or under usual illumination levels the device can work in high-injection conditions, the occupancy change of valence band bulk holes gives rise to an additional capacitance per unit volume C_p, being p the hole concentration and E_{F_p} the hole quasi-Fermi level:

$$C_p = -q^2 \frac{dp}{dE_{F_p}}. \tag{7}$$

Importantly, as illustrated in Figure 3, C_{dl} is dominant at reverse and low forward bias regions but surpassed by $C_{n,p}$ as forward bias increases. For instance, in dark and at

short-circuit, Figure S3f evidences the predominant depletion layer capacitance as it follows its $C_{dl} \propto T^{-1/2}$ trend from equation 2.

The equivalent circuit of Figure 5a models the solar cell operation through the contribution of two resistive elements accounting for the individual capture of holes and electrons by the recombination centers. Surface recombination centers govern then the recombination flux through R_n and R_p, which are spatially confined at the interface, while the AC response is coupled with bulk chemical capacitances of equations 6 and 7. Consequently, the SRH carrier lifetime results by considering the separate contributions from the capture times of each carrier type as [33]

$$\tau_{SRH} = \tau_n + \tau_p = R_n C_n + R_p C_p . \quad (8)$$

Figures S7-S9 present the impedance plots with experimental data and fittings for the three solar cells under study, as well as the resulting fitting parameters for the respective V_{oc} values. The behavior of τ_{SRH} values are summarized in Figure 5b, showing that carrier lifetime is larger for V_2O_5-based cells. This is in agreement with the results of the QSSPC technique (Figure S5), both in order of magnitude and general trend. From this comparison, and considering individual lifetime constant values (Figures S7e, S8f and S9d), it is assumed that the longer time constant corresponds to minority carriers (holes) and the shorter to the majority carriers (given that it is a n-Si base). The superior performance of V_2O_5–based cells is then connected to the reduction in surface recombination by enhanced passivation that, consequently, produces higher open-circuit voltages. Nearly one order of magnitude improvement in lifetime is observed (~200 μs) for f-V_2O_5 in comparison to textured devices. In terms of effective recombination velocity, approximated as $S_{eff} \approx L/\tau_{SRH}$ being L the absorber n-Si thickness, one can calculate that S_{eff} ~140 cm s^{-1} (f-V_2O_5), S_{eff} ~1300 cm s^{-1} (t-V_2O_5), and S_{eff} ~2600 cm s^{-1} (t-MoO_3), signaling the effectiveness of the passivation strategy. By comparing S_{eff} corresponding to laser firing rear structures (t-V_2O_5 and t-MoO_3), one can observe the beneficial effect of the textured V_2O_5 hole-selective contact. After changing the structure of both rear and front contacts (f-V_2O_5) the performance enhancement is even larger.

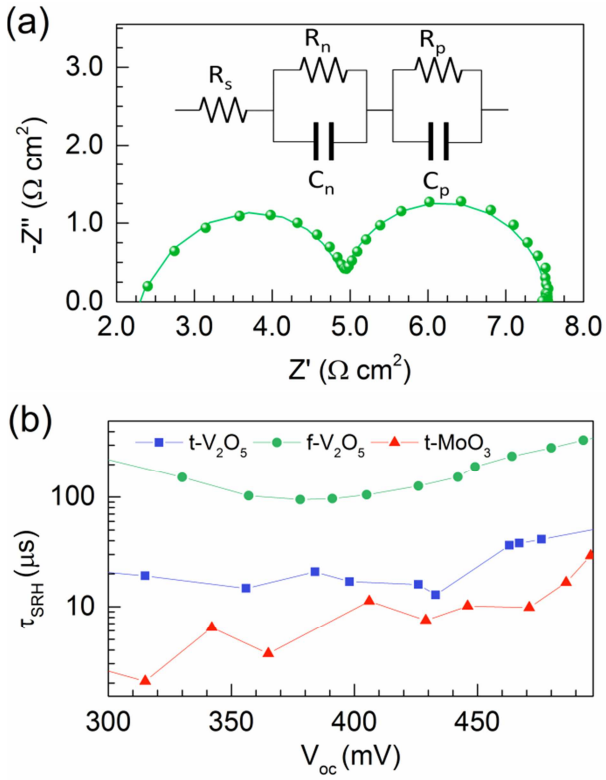

Figure 5: (a) Nyquist plot for the experimental *IS* results (dots) of f-V_2O_5 sample at $V_{oc} = 633$ mV with its respective fitting (solid line) to the equivalent circuit (inset). (b) Total carrier lifetime for the studied samples, as indicated.

Regarding the chemical capacitance, it is known that it follows an exponential dependence with the applied voltage V (or V_{oc}) of the form $C_n \propto \exp(qV/k_BT)$ [16, 34]. Accordingly, from equations 6 and 7 and taking into account how the splitting of the quasi-Fermi levels depends on the carrier concentration [36], the capacitance per unit area can be expressed as [33]

$$C_{n,p} = \frac{q^2 L_{n,p}}{2k_BT} \frac{n_i^2 \exp\left[\left(E_{F_n} - E_{F_p}\right)/k_BT\right]}{\sqrt{\left(N_D/2\right)^2 + n_i^2 \exp\left[\left(E_{F_n} - E_{F_p}\right)/k_BT\right]}}. \quad (9)$$

Here n_i is the intrinsic carrier concentration, and $L_{n,p}$ stands for the effective bulk length (normal to the interface direction) of the region where the electron (or hole) occupation changes take place. This latter parameter reflects the consequent geometric differences between electrons and holes bulk capacitive behaviors due to its different recombination rates and diffusion lengths.

Moreover, the quasi-Fermi levels match the V_{oc} energy (i.e. $qV_{oc} = E_{F_n} - E_{F_p}$, which is the free energy of an electron–hole pair) if infinite carrier mobility, homogeneous carrier density profiles and perfectly selective contacts are considered as good approximations [33]. Thus $C_{n,p}(V_{oc})$ plotting should exponentially grow. Such behavior is clearly observed in Figures S7c, S8d, and S9b where the capacitances $C_{p,n}$ obtained

from fitting are plotted as a function of V_{oc}.

In addition, the capacitive data of Figures S7c, S8d, and S9b were also fitted to equation 9 by using the parameters listed in Table ST2. By considering plausible n_i levels and carrier concentrations similarly to those of Table T1, L_p values of hundreds of micrometers were obtained for the three samples. On the other hand, L_n of around tens of micrometers were obtained for the textured samples. Interestingly, from equation 9 a change in exponential slope from q/k_BT to $q/2k_BT$ is expected if logarithm scaled capacitance is plotted as a function of $E_{F_n} - E_{F_p}$. As also pointed in Figures S7c, S8d, and S9b, the simulated change in exponential slope from q/k_BT to $q/2k_BT$ can be appreciated in good agreement with the experimental data.

4. Conclusions

In summary, transition metal oxides V_2O_5 and MoO_3 have been electrically studied as hole selective contacts in heterojunction c-Si solar cells. It has been shown that V_2O_5–based devices have better performance than those using MoO_3. While textured devices using V_2O_5 exhibit larger short-circuit currents, it was observed that flat solar cell architectures permit for a significant increase in passivation of the V_2O_5/n-Si interface. This strategy allows for open-circuit voltage values reaching 662 mV. Such improvement has been supported by the exploration of the depletion layer features and the evaluation of minority carrier lifetimes. For the latter, a protocol based on *IS* analysis has been proposed, also revealing the important role of capacitive mechanisms in the performance of the TMO/n-Si cells. In addition, some considerations on the energy band diagram have been discussed, although some detailed aspects (such as the magnitude of dipoles involved) need to be determined in future work. Therefore, a more thorough understanding of the TMO/n-Si interface and the energetics involved could result in significant improvements for this kind of novel c-Si solar cells.

Supporting Information

Supporting Information is available from the Wiley Online Library or from the author.

Acknowledgements

We thank financial support by Ministerio de Economía y Competitividad (MINECO) of Spain under projects MAT2016-76892-C3-1-R, ENE2013-48629-C4-1-R and ENE2014-56237-C4-1-R, and also from Generalitat Valenciana (Prometeo/2014/020). O. A. acknowledges Generalitat Valenciana for a grant (GRISOLIAP2014/035). L. G. G. acknowledges Mexico's grant program CONACyT for a grant.

References

[1] M.A. Green, K. Emery, Y. Hishikawa, W. Warta, E.D. Dunlop, D.H. Levi, A.W.Y. Ho-Baillie, Solar Cell Efficiency Tables (version 49), Progress in Photovoltaics: Research and Applications, 25 (2017) 3-13.

[2] C. Battaglia, A. Cuevas, S. De Wolf, High-efficiency crystalline silicon solar cells: status and perspectives, Energy Environ. Sci., 9 (2016) 1552-1576.

[3] S. De Wolf, M. Kondo, Nature of doped a-Si:H/c-Si interface recombination, J. Appl. Phys., 105 (2009) 103707.

[4] C. Battaglia, X. Yin, M. Zheng, I.D. Sharp, T. Chen, S. McDonnell, A. Azcatl, C. Carraro, B. Ma, R. Maboudian, R.M. Wallace, A. Javey, Hole Selective MoOx Contact for Silicon Solar Cells, Nano Lett., 14 (2014) 967-971.

[5] J. Bullock, M. Hettick, J. Geissbühler, A.J. Ong, T. Allen, Carolin M. Sutter-Fella, T. Chen, H. Ota, E.W. Schaler, S. De Wolf, C. Ballif, A. Cuevas, A. Javey, Efficient Silicon Solar Cells with Dopant-Free Asymmetric Heterocontacts, Nat. Energy, 1 (2016) 15031.

[6] J. Meyer, S. Hamwi, M. Kröger, W. Kowalsky, T. Riedl, A. Kahn, Transition Metal Oxides for Organic Electronics: Energetics, Device Physics and Applications, Adv. Mater., 24 (2012) 5408-5427.

[7] F. Wang, Z.a. Tan, Y. Li, Solution-Processable Metal Oxides/Chelates as Electrode Buffer Layers for Efficient and Stable Polymer Solar Cells, Energy Environ. Sci., 8 (2015) 1059-1091.

[8] J. Geissbühler, J. Werner, S. Martin de Nicolas, L. Barraud, A. Hessler-Wyser, M. Despeisse, S. Nicolay, A. Tomasi, B. Niesen, S. De Wolf, C. Ballif, 22.5% Efficient Silicon Heterojunction Solar Cell with Molybdenum Oxide Hole Collector, Appl. Phys. Lett., 107 (2015) 081601.

[9] James Bullock, Christian Samundsett, Andres Cuevas, Di Van, Y. Wan, T. Allen, Proof-of-concept p-type silicon solar cells with molybdenum oxide partial rear contacts, in: 2015 IEEE 42nd Photovoltaic Specialist Conference (PVSC), IEEE, 2015.

[10] L.G. Gerling, S. Mahato, A. Morales-Vilches, G. Masmitja, P. Ortega, C. Voz, R. Alcubilla, J. Puigdollers, Transition Metal Oxides as Hole-Selective Contacts in Silicon Heterojunctions Solar Cells, Sol. Energy Mater. Sol. Cells, 145, Part 2 (2016) 109-115.

[11] M. Bivour, J. Temmler, F. Zähringer, S. Glunz, M. Hermle, High Work Function Metal Oxides for the Hole Contact of Silicon Solar Cells, in: 2016 IEEE 43rd Photovoltaic Specialists Conference (PVSC), IEEE, Portland, OR, USA, 2016, pp. 0215-0220.

[12] W. Wu, J. Bao, X. Jia, Z. Liu, L. Cai, B. Liu, J. Song, H. Shen, Dopant-Free Back Contact Silicon Heterojunction Solar Cells Employing Transition Metal Oxide Emitters, Phys. Status Solidi RRL, 10 (2016) 662-667.

[13] J. Bullock, A. Cuevas, T. Allen, C. Battaglia, Molybdenum oxide MoOx: A versatile hole contact for silicon solar cells, Appl. Phys. Lett., 105 (2014) 232109.

[14] M. Colina, A.B. Morales-Vilches, C. Voz, I. Martín, P.R. Ortega, R. Alcubilla, Low Surface Recombination in Silicon-Heterojunction Solar Cells With Rear Laser-Fired Contacts From Aluminum Foils, IEEE J. Photovoltaics, 5 (2015) 805-811.

[15] L.G. Gerling, C. Voz, R. Alcubilla, J. Puigdollers, Origin of Passivation in Hole-Selective Transition Metal Oxides for Crystalline Silicon Heterojunction Solar Cells, J. Mater. Res., 32 (2016) 260-268.

[16] S.M. Sze, K.K. Ng, Physics of Semiconductor Devices, 3rd ed., John Wiley & Sons, Hoboken, New Jersey, USA, 2007.

[17] G.A. Samara, Temperature and Pressure Dependences of the Dielectric Constants of Semiconductors, Phys. Rev. B, 27 (1983) 3494-3505.

[18] M. Bivour, B. Macco, J. Temmler, W.M.M. Kessels, M. Hermle, Atomic Layer Deposited Molybdenum Oxide for the Hole-selective Contact of Silicon Solar Cells, Energy Procedia, 92 (2016) 443-449.

[19] R. Herberholz, M. Igalson, H.W. Schock, Distinction Between Bulk and Interface States in $CuInSe_2$/CdS/ZnO by Space Charge Spectroscopy, J. Appl. Phys., 83 (1998) 318-325.

[20] T. Walter, R. Herberholz, C. Müller, H.W. Schock, Determination of Defect Distributions from Admittance Measurements and Application to $Cu(In,Ga)Se_2$ Based Heterojunctions, J. Appl. Phys., 80 (1996) 4411-4420.

[21] I. Mora-Sero, G. Garcia-Belmonte, P.P. Boix, M.A. Vazquez, J. Bisquert, Impedance spectroscopy characterisation of highly efficient silicon solar cells under different light illumination intensities, Energy Environ. Sci., 2 (2009) 678-686.

[22] A.F. Braña, E. Forniés, N. López, B.J. García, High Efficiency Si Solar Cells Characterization Using Impedance Spectroscopy Analysis, Journal of Physics: Conference Series, 647 (2015) 012069.

[23] J.V. Li, A.F. Halverson, O.V. Sulima, S. Bansal, J.M. Burst, T.M. Barnes, T.A. Gessert, D.H. Levi, Theoretical analysis of effects of deep level, back contact, and absorber thickness on capacitance–voltage profiling of CdTe thin-film solar cells, Solar Energy Materials and Solar Cells, 100 (2012) 126-131.

[24] O. Almora, L. Vaillant-Roca, A. Bosio, Electrical Characterizations of CdTe/CdS Poly-Crystalline Thin Film Solar Cells, Rev. Cuba Fis., 31 (2014) 66-70.

[25] P.J. Sebastian, M.E. Calixto, R.N. Bhattacharya, R. Noufi, CIS and CIGS Based Photovoltaic Structures Developed from Electrodeposited Precursors, Sol. Energy Mater. Sol. Cells, 59 (1999) 125-135.

[26] T. Eisenbarth, T. Unold, R. Caballero, C.A. Kaufmann, H.-W. Schock, Interpretation of Admittance, Capacitance-Voltage, and Current-Voltage Signatures in $Cu(In,Ga)Se_2$ Thin Film Solar Cells, J. Appl. Phys., 107 (2010) 034509.

[27] P.P. Boix, J. Ajuria, I. Etxebarria, R. Pacios, G. Garcia-Belmonte, J. Bisquert, Role of ZnO Electron-Selective Layers in Regular and Inverted Bulk Heterojunction Solar Cells, J. Phys. Chem. Lett., 2 (2011) 407-411.

[28] O. Almora, C. Aranda, E. Mas-Marzá, G. Garcia-Belmonte, On Mott-Schottky Analysis Interpretation of Capacitance Measurements in Organometal Perovskite Solar Cells, Appl. Phys. Lett., 109 (2016) 173903.

[29] Y. Guo, J. Robertson, Origin of the High Work Function and High Conductivity of MoO_3, Appl. Phys. Lett., 105 (2014) 222110.

[30] B. Ghosh, Electrical Contacts for II–VI Semiconducting Devices, Microelectron. Eng., 86 (2009) 2187-2206.

[31] V.F. Lvovich, Impedance Spectroscopy. Applications to Electrochemical and Dielectric Phenomena, John Wiley & Sons, Inc., Hoboken, New Jersey, 2012.

[32] R.A. Sinton, A. Cuevas, Contactless Determination of Current–Voltage Characteristics and Minority-Carrier Lifetimes in Semiconductors from Quasi-Steady-State Photoconductance Data, Appl. Phys. Lett., 69 (1996) 2510-2512.

[33] I. Mora-Seró, Y. Luo, G. Garcia-Belmonte, J. Bisquert, D. Muñoz, C. Voz, J. Puigdollers, R. Alcubilla, Recombination Rates in Heterojunction Silicon Solar Cells Analyzed by Impedance Spectroscopy at Forward Bias and Under Illumination, Sol. Energy Mater. Sol. Cells, 92 (2008) 505-509.

[34] J. Bisquert, Nanostructured Energy Devices: Equilibrium Concepts and Kinetics, CRC Press Taylor & Francis Group, Boca Raton, 2014.

[35] J. Bisquert, D. Cahen, G. Hodes, S. Rühle, A. Zaban, Physical Chemical Principles of Photovoltaic Conversion with Nanoparticulate, Mesoporous Dye-Sensitized Solar Cells, J. Phys. Chem. B, 108 (2004) 8106-8118.

[36] R. Brendel, Thin-Film Crystalline Silicon Solar Cells: Physics and Technology, Wiley-VCH Verlag GmbH & Co. KGaA, Weinheim, 2003.